RESEARCH ARTICLE

ADVANCED OPTICAL MATERIALS
www.advopticalmat.de

Anion Effect on the Thermometric Properties of Near-Infrared Emitting Mn^{5+}-Activated $Sr_5(PO_4)_3X$ (X = F, Cl, Br) Apatite Phosphors

Michele Back, Jacopo Cangiotti, Jonas Stadulis, Arturas Katelnikovas, Mikhail G. Brik, Pietro Riello, and Aleksej Zarkov**

Near-infrared emitting Mn^{5+}-activated phosphors are recently recognized as promising thermal sensors for biological applications. However, guidelines to predict suitable hosts with optimal temperature sensing ability are still missing. In this view, the indirect effect of the different halides on the $3d^2$ electrons of the Mn^{5+} ions in different $Sr_5(PO_4)_3X$ apatites (X = F, Cl, and Br) is deeply investigated through a combined experimental and theoretical approach. The temperature dependence of the PL and decay curves allows to simultaneously get information about the electron-phonon coupling and the potential application as optical thermometers, showing promising results in terms of relative sensitivity. Boltzmann-based and lifetime-based thermometry ensure a unique reliability, and the simultaneous use of the ratio between the emission originating from the $^3T_1$ and ^1E excited states and the split components of the ^1E (E_1 and E_2) state allows to enlarge the temperature range of applicability of the thermometers from cryogenic to high temperature. The local $[PO_4]^{3-}$ tetrahedral geometry in the halide apatites drives their thermometric properties, showing interesting results in terms of sensitivity, particularly for the bromide $Sr_5(PO_4)_3Br:Mn^{5+}$ phosphor. Moreover, the high quantum efficiencies estimated at room temperature support the potential use in real applications of this family of NIR phosphors.

1. Introduction

Mn^{5+} ions stabilized in insulating host materials have been attracting a lot of interest for a long time due to their optical properties exploited for pigments and investigated as promising near-infrared (NIR) lasers. Indeed, intense and bright colours ranging from blue to green can be obtained by incorporating Mn^{5+} into tetrahedral sites of phosphates, vanadates, and arsenides.[1–5] Mn^{5+} ions are characterized by a $3d^2$ electron configuration, isoelectronic to Ti^{2+}, V^{3+}, Cr^{4+}, and Fe^{6+}. As in the case of the small Fe^{6+}, Mn^{5+} ions have a strong preference for the tetrahedral MnO_4^{3-} configuration.[6] Since the first detailed spectroscopic report about the luminescence of Mn^{5+} ions in Ca_2PO_4Cl spodiosite and $Ca_5(PO_4)_3Cl$ apatite by J. D. Kingsley et al. 60 years ago,[7] Mn^{5+}-activated phosphors were thoroughly investigated demonstrating the presence of a strong charge transfer in the absorption/excitation

M. Back, J. Cangiotti, P. Riello
Department of Molecular Sciences and Nanosystems
Ca' Foscari University of Venice
Via Torino 155, Mestre – Venice 30172, Italy
E-mail: michele.back@unive.it

J. Stadulis, A. Katelnikovas, A. Zarkov
Institute of Chemistry
Faculty of Chemistry and Geosciences
Vilnius University
Naugarduko 24, Vilnius LT-03225, Lithuania
E-mail: aleksej.zarkov@chf.vu.lt

The ORCID identification number(s) for the author(s) of this article can be found under https://doi.org/10.1002/adom.202503109

DOI: 10.1002/adom.202503109

M. G. Brik
School of
Optoelectronic Enginee
ring & CQUPT-BUL Innovation Institute
Chongqing University of Posts and Telecommunications
Chongqing 400065, China

M. G. Brik
Centre of Excellence for Photoconversion
Vinča Institute of Nuclear Sciences – National Institute of the Republic of Serbia
University of Belgrade
Belgrade 11351, Serbia

M. G. Brik
Institute of Physics
University of Tartu
W. Ostwald Str. 1, Tartu 50411, Estonia

M. G. Brik
Institute of Physics
Jan Długosz University
Częstochowa PL-42200, Poland

M. G. Brik
Academy of Romanian Scientists
3 Ilfov, Bucharest 050044, Romania

spectra in addition to the typical d-d transitions.[8–16] Considering the ionic radii, the oxidation state, and the tetrahedral coordination, the most common hosts reported so far are phosphates and vanadates. However, silicates and germanates such as Y_2SiO_5,[17] M_2SiO_4 with M = Ca, Sr, Ba,[12,18] and $Ba_2(Si,Ge)O_4$[19] or aluminates such as $YAlO_3$ perovskite[20,21] were also reported. The sharp NIR emission originated from the spin-forbidden $^1E \rightarrow {}^3A_2$ transition makes these materials particularly appealing for NIR lasers[22–26] with $Ba_3(VO_4)_2$:Mn^{5+} being the first example of Mn^{5+}-activated material showing laser action.[27] More recently, a renewed interest has been demonstrated in this family of phosphors for applications as NIR-II contrast agents,[28] narrow-band NIR LEDs,[29] and luminescent thermal sensing.[19,30–37]

The use of luminescence signals to probe temperature is particularly promising due to the possibility of a remote technology, with suitable sensitivity, good thermal resolution, reproducibility, and unique reliability.[38–40] Among the wide variety of techniques for thermal sensing, involving the use of a peak broadening, shift, intensity, or lifetime variation, the use of the ratiometric concept employing the ratio between the signals from two excited states or the temperature dependence lifetimes of the excited states are well recognized among the most reliable ones. The so-called Boltzmann thermometers rely on the Boltzmann law between the populations of two thermally coupled excited states, which have been widely investigated for materials doped with Er^{3+},[41,42] Nd^{3+},[43,44] and Cr^{3+},[45,46] demonstrating their reliable applicability in a wide range of technological fields. Moreover, the interest in temperature sensing through luminescence signals is becoming particularly important not only from an academic point of view, with examples of applications to probe intracellular temperature,[47,48] temperature of catalytic processes,[49–51] and in microfluidic,[52] to name a few.

In this framework, Mn^{5+}-doped phosphors have been recently recognized as promising thermal probes working in the biological windows (BWs) with the additional advantage with respect to other NIR emitting materials, such as Nd^{3+} or Er^{3+}-doped systems, to be characterized by broad and efficient excitations also falling into the BWs, particularly suitable for biological applications. In addition, Mn^{5+}-activated nanoparticles have been demonstrated to resist photochemical degradation.[28,53] However, no general rules for the prediction and design of effective Mn^{5+}-activated phosphors for NIR thermometry have been reported so far, remaining a challenge. With the aim to bridge this gap, in this work we investigate the correlation between the local tetrahedral MnO_4^{3-} site, the electronic structure, and the thermometric properties of the $Sr_5(PO_4)_3X$:Mn^{5+} (X = F, Cl, Br) halide apatites, considered as prototypes. A combined experimental and theoretical approach is used to try to disclose the local structure-optical relationship, allowing the optimization of the sensitivity and the expansion of the temperature range of applicability.

2. Results and Discussion

With the aim of optimizing the luminescent properties, at first, a series of $Sr_5(P_{1-y}Mn_yO_4)_3X$ phosphors (X = F, Cl, and Br) with y = 0.0000, 0.0010, 0.0100, 0.0125, 0.0166, 0.0250, and 0.0500 was prepared by molten-salt synthesis. The stabilization of the strontium halogen apatite structure was confirmed for all samples by X-ray powder diffraction (XRPD) (Figure S1a-c, Supporting Information) while the photoluminescence emission (PL) intensity signals as a function of the Mn content showed that the best PL is obtained for the samples with y = 0.0166 in bromide, chloride, and fluoride samples (from now labelled as $Sr_5(PO_4)_3X$:Mn^{5+}). These materials were considered as prototypes to evaluate the effect of the local crystal structure in these series of halide apatites on the thermometric performance in the NIR window.

2.1. Crystalline Structure and Local Tetrahedral Site Investigation

The XRPD patterns of the three apatites show a good matching with the ICSD references of the hexagonal structure ($P6_3/m$ space group, No. 176) in terms of diffraction peaks position (ICSD#95737 for $Sr_5(PO_4)_3F$, ICSD#2089 for $Sr_5(PO_4)_3Cl$, and ICSD#253054 for $Sr_5(PO_4)_3Br$), although an evident difference in terms of relative peak intensities for the fluoride and chloride apatites is observed (**Figure 1a-c**). In order to elucidate this behavior, Rietveld refinements, including the March-Dollase approach to consider possible preferred orientations along the (001) direction, were performed (see Experimental Section).[54,55] A March-Dollase parameter of 1.00, 1.12, and 1.60 was obtained through the Rietveld refinement for the bromide, chloride, and fluoride samples, respectively. The *c*-axis preferential orientation suggested for the fluoride and chloride agrees with the conventional habitus adopted by the apatite crystals, as confirmed by the SEM images of the chloride and fluoride apatites (Figure S2a,b, Supporting Information). It is worth noting that the apatite structures are characterized by a single tetrahedral $[PO_4]^{3-}$ site for the substitution of Mn^{5+} ions (Figure 1d,e). Considering the structures obtained from the Rietveld refinements (see the parameters estimated in Tables S1-S3, Supporting Information), the average <P—O> bond length, the polyhedral distortion index *D*, and the T_d-distortion angle δ of the tetrahedral T_d sites were calculated as:[4,56]

$$D = \frac{1}{n}\sum_{i=1}^{n}\frac{|l_i - l_{av}|}{l_{av}} \quad (1)$$

$$\delta = \frac{1}{6}\sum_{i=1}^{6}|2\theta_i - 2\theta_t| \quad (2)$$

where $n = 4$ for the tetrahedral sites, l_i is the bond length between the central cation and the i^{th} coordination ligand, l_{av} = <P—O> is the average bond length, and $2\theta_t$ is the tetrahedral angle. The values calculated for the apatites are summarized in **Table 1**. The distortion index *D* shows a relative increase moving from bromide to chloride and fluoride. On the other hand, the deviation from the T_d geometry in terms of distortion angle δ evidences a different behavior with an increasing value moving from bromide to fluoride and finally chloride.

2.2. Optical Properties and Electronic Structure: Tanabe-Sugano Diagram and Exchange Charge Model

Figure 2a shows the room temperature PL and photoluminescence excitation (PLE) spectra of Mn^{5+} ions in the samples.

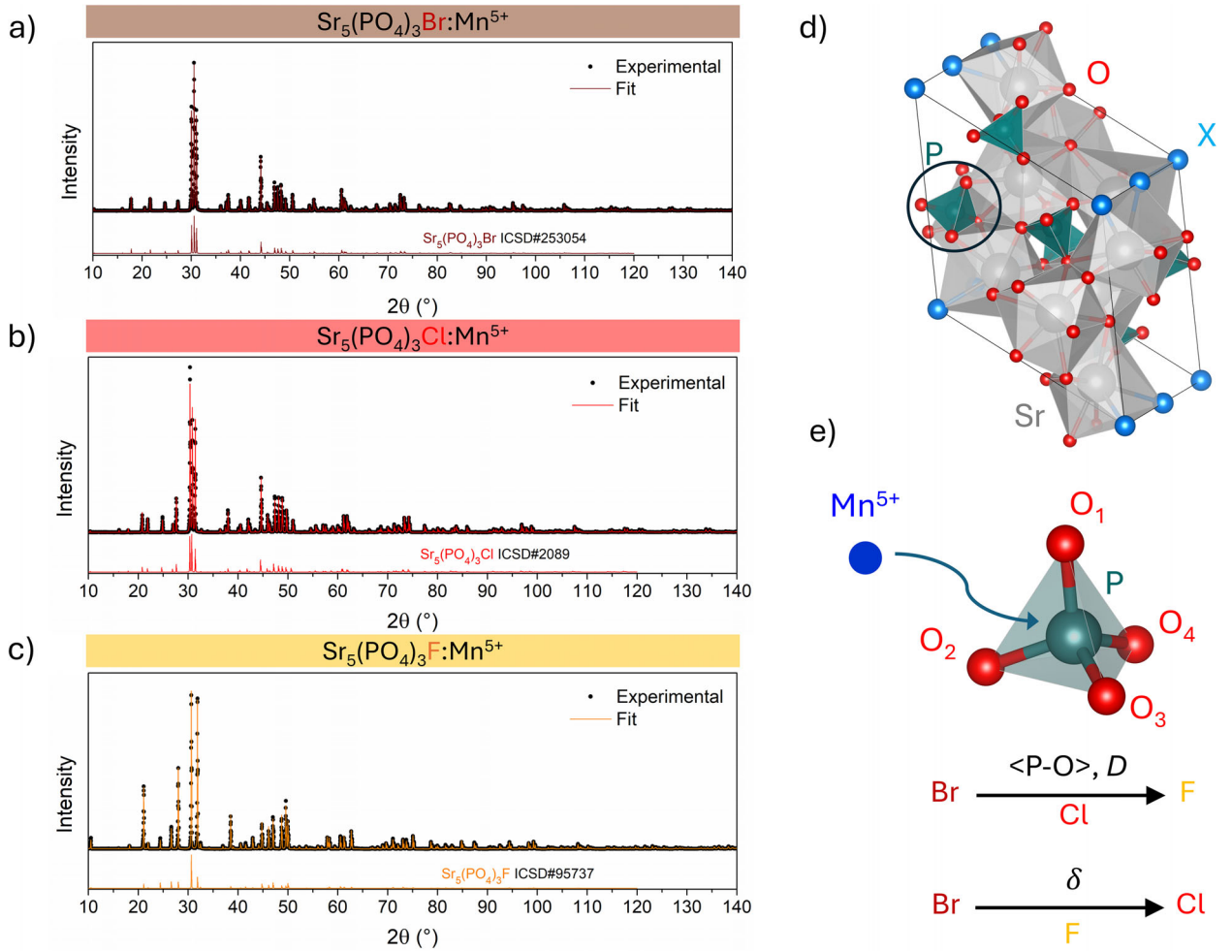

Figure 1. a-c) XRPD pattern and Rietveld refinements of the $Sr_5(PO_4)_3X$ apatites along with ICSD references. d) Crystalline structure of $Sr_5(PO_4)_3X$ apatites. e) Sketch of the local tetrahedral $[PO_4]^{3-}$ site for the stabilization of Mn^{5+} ions along with the average <P—O> bond length, the distortion index *D*, and the distortion angle δ as a function of the halide in the apatite structures.

The sharp PL spectra are characteristic of the strong crystal field due to the $^1E \rightarrow {}^3A_2$ transitions. The ground state ($^3A_2$) is non-degenerate, derived from the e^2 strong field configuration, while the ^1E excited state has an e^2 configuration which can be split into two components E_1 (E_{z^2}) and E_2 ($E_{x^2} - E_{y^2}$) by the low symmetry ligand field. On the other hand, the excitation spectra are composed by a series of broadbands with at least three main components due to the $^3A_2 \rightarrow {}^3T_2$, $^3A_2 \rightarrow {}^3T_1$ transitions and charge transfer (CT) band around 900, 600, and 300 nm, respectively. It is worth mentioning that all the samples not only emit in the second biological window at ≈1200 nm, but they can also be efficiently excited in the first biological window[57] (from now on, all the measurements are performed exciting at 700 nm). The PL decay curves (Figure 2b) can be fit by a single exponential showing ^1E excited state lifetimes in the order of hundreds of microseconds (399, 386, and 498 µs for bromide, chloride, and fluoride apatite, respectively) in agreement with the typical values reported in the literature. On the other hand, as summarized in Figure 2c, remarkable internal quantum efficiencies (IQE) of 46% ± 5%, 47% ± 5% and 66% ± 5% are obtained at room temperature for $Sr_5(PO_4)_3F:Mn^{5+}$, $Sr_5(PO_4)_3Cl:Mn^{5+}$, and $Sr_5(PO_4)_3Br:Mn^{5+}$, respectively, suggesting effective potential for practical applications.

Table 1. Polyhedral distortion index *D*, δ T_d-distortion angle, crystal field strength *Dq*, Racah parameters *B* and *C*, *C*/*B* and *Dq*/*B* values for the Mn^{5+}-activated halide apatites.

Sample	*D*	δ [°]	*Dq* [cm^{-1}]	*B* [cm^{-1}]	*C* [cm^{-1}]	*C*/*B*	*Dq*/*B*
$Sr_5(PO_4)_3F$	0.048	2.71	1118	438	2614	5.96	2.55
$Sr_5(PO_4)_3Cl$	0.030	4.31	1101	485	2405	4.96	2.27
$Sr_5(PO_4)_3Br$	0.015	2.30	1067	508	2304	4.53	2.10

The analysis of the crystalline environment effect on the Mn^{5+} electrons can be performed by means of the Tanabe-Sugano theory by employing the diagram for the $3d^2$ configuration in a tetrahedral site corresponding to the Tanabe-Sugano diagram for the $3d^8$ octahedral coordination. In this framework, the crystal field strength *Dq* and the Racah parameters *B* and *C* can be

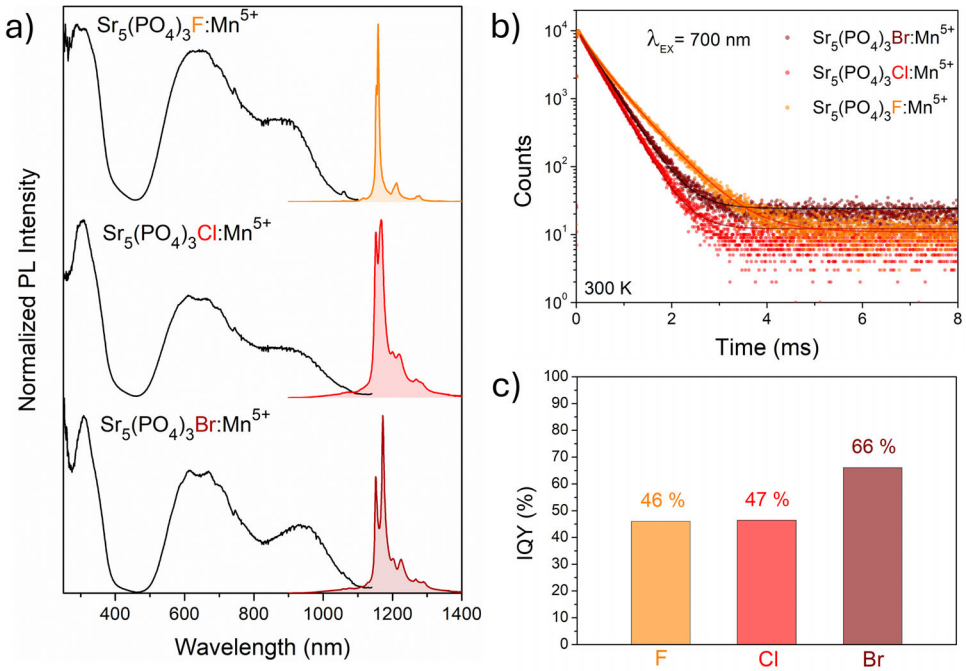

Figure 2. a) PL and PLE spectra, b) PL decay curves exciting at 700 nm and collecting the ^{1}E emission with the single exponential fit, and c) IQY of the Mn^{5+}-doped $Sr_5(PO_4)_3X$ (X = F, Cl, and Br) apatite phosphors.

evaluated from the spectroscopic analysis using the following equations:

$$10Dq = E\left({}^3A_2 \rightarrow {}^3T_2\right) \tag{3}$$

$$B = \frac{x^2 - 10x}{15\,(x-8)}\ Dq\ with\ x = \frac{E\left({}^3A_2 \rightarrow {}^3T_1\right) - E\left({}^3A_2 \rightarrow {}^3T_2\right)}{Dq} \tag{4}$$

$$C = 0.5\left[E\left({}^3A_2 \rightarrow {}^1E\right) - 10Dq - 8.5B + 0.5\sqrt{400Dq^2 + 40DqB + 49B^2}\right] \tag{5}$$

A clear blue shift of the low energy PLE broadband assigned to the $^3A_2 \rightarrow {}^3T_2$ transition is observed moving from the bromo- to the chloro- and fluoro-apatite (Figure 2a) and the same blue shift can be recognized in the ^{1}E emissions (8632, 8565, and 8532 cm^{-1} for $Sr_5(PO_4)_3F$, $Sr_5(PO_4)_3Cl$, and $Sr_5(PO_4)_3Br$, respectively). It is interesting to recognize the direct correlation between the energy of the ^{1}E position and the distortion index D. The crystal field strength Dq and Racah parameters B and C estimated are also reported in Table 1, showing a relative increase in the Dq/B values moving from the bromide (2.10) to chloride (2.27), and finally fluoride (2.55) samples.

As demonstrated for other transition metal ions such as Cr^{3+},[58,59] an accurate comparison of the effect of the crystal field on their energy levels in different hosts based on the Tanabe-Sugano theory can be achieved only by considering the diagrams built for the specific C/B. The values estimated evidence a large deviation from the original value of 4.50, in particular for the chloride (C/B = 4.96) and fluoride (C/B = 5.96) samples, in agreement with the larger deviation from the ideal tetrahedral sites demonstrated in terms of both D and δ parameters. Based on the values estimated spectroscopically, the Tanabe-Sugano diagrams for the corresponding C/B values of the $3d^2$ in the tetrahedral sites (corresponding to the $3d^8$) of the strontium halogen $Sr_5(PO_4)_3X$ apatites are calculated (**Figure 3**). Considering the Dq/B values for the Tanabe-Sugano diagrams plotted for the corresponding C/B, it is evident that the energy of the ^{1}E state increases for Mn^{5+} ions moving from bromide to chloride and fluoride, in agreement with the PL spectra, and the relative energy gap between the ^{1}E and $^3T_2$ levels is also changing but only slightly with respect to the large change predicted by considering the diagram built with C/B = 4.50.

It must be pointed out that the assignment of the energy position of the broadbands related to the $^3A_2 \rightarrow {}^3T_2$ and $^3A_2 \rightarrow {}^3T_1$ transitions is not trivial, leading to values of the crystal field strength Dq and the Racah parameters B and C that are difficult to compare reliably with respect to the literature. In addition, the Tanabe-Sugano theory was developed to describe the splitting of the terms of the free ions for ideal symmetric octahedral or tetrahedral fields (generally defined as cubic crystal fields) being not suitable when large distortions are present. To overcome this limit and go deeper in the investigation of the effect of the local symmetry on the energy levels of Mn^{5+} ions, the energy levels and the Dq, B, and C parameters were calculated by means of the exchange charge model (ECM) of the CF theory[60–62] by analysing the experimental spectra and considering the local geometry obtained through the crystalline structure investigation. The results are shown in Figure S3 (Supporting Information), showing a good match between the spectra and the energy levels calculated. Tables S4 and S5 (Supporting Information)

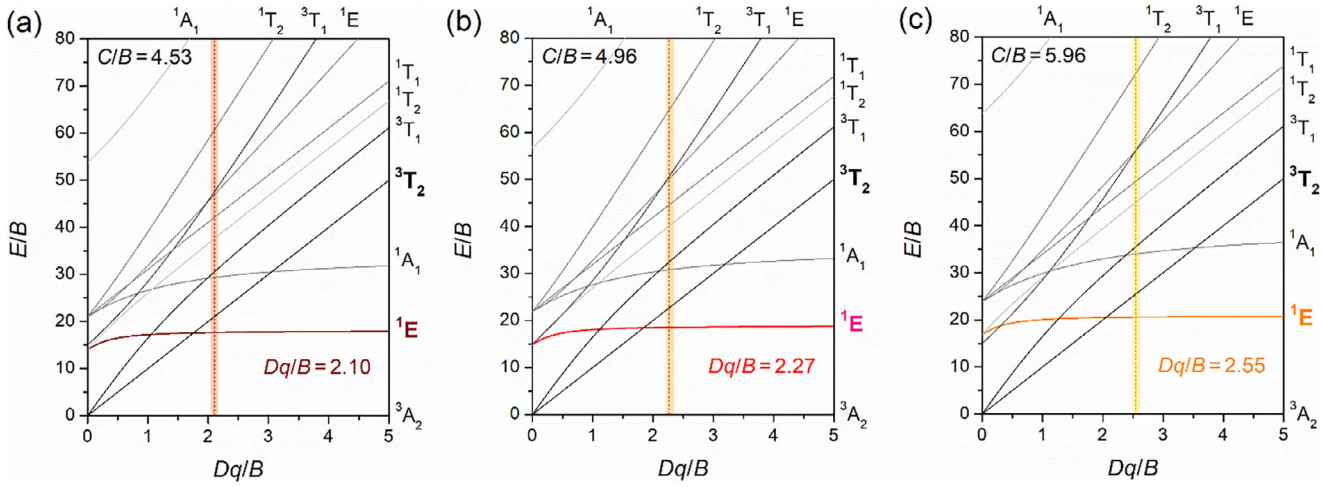

Figure 3. Calculated $3d^8$ Tanabe-Sugano diagram for the proper C/B values of Mn^{5+} in tetrahedral sites for a) $Sr_5(PO_4)_3Br:Mn^{5+}$, b) $Sr_5(PO_4)_3Cl:Mn^{5+}$, and c) $Sr_5(PO_4)_3F:Mn^{5+}$.

summarize the crystal field parameters, the Racah parameters, and the energy levels calculated for Mn^{5+} ions in the $Sr_5(PO_4)_3X$ apatites.

It is worth noting that for an ideal tetrahedral site, the B_4^4 value is 5 times B_4^0 if the crystal field parameters are calculated in the Stevens normalization. However, the B_4^4/B_4^0 ratio is only slightly deviating from this value in the case of the chloride apatite ($B_4^4/B_4^0 \approx 4$), but it is strongly deviating in the case of the fluoride and bromide samples ($B_4^4/B_4^0 \approx 11$).

Due to the unshielded electrons involved in the optical transitions of $3d^2$ transition metal ions, the electron-phonon coupling (EPC) plays a critical role in the thermal behavior of their luminescence. To account for the EPC interaction, an effective phonon energy is usually considered. The temperature dependence of the spectral emission shift of the $^1E \rightarrow {}^3A_2$ transition in the apatites is investigated in the temperature range of 77–400 K (**Figure** 4a-c). As the temperature increases from 77 to 400 K, the PL spectra red shift.

The red shift of the zero phonon line (ZPL) ΔE_Z is caused by the quadratic interactions of the electrons with acoustic phonons and can be described in the framework of the Debye model as:[63]

$$\Delta E_Z(T) = \alpha_{EP}\left(\frac{T}{\theta_D}\right)^4 \int_0^{\theta_D/T} \frac{x^3}{e^x - 1} dx \quad (6)$$

where θ_D is the Debye temperature, $\alpha_{EP} = \frac{3k_B\theta_D}{2}\frac{w}{w+1}$ is the electron-phonon coupling parameter (in cm^{-1}), and w is the quadratic coupling constant ($w > -1$). A Debye temperature θ_D of 700 K, 600 K, and 720 K can be estimated from the fit of the emission shift for the fluoride, chloride, and bromide-based apatites, respectively (Figure 4d-f). Consequently, the cutoff frequency ω_{cutoff} and the effective phonon energy of $Sr_5(PO_4)_3X$ apatites are estimated as $\hbar\,\omega_{cutoff} = k_B \cdot \theta_D$, giving values of 487 cm^{-1}, 417 cm^{-1}, and 500 cm^{-1} for X = F, Cl, and Br, respectively. These values are slightly lower than those reported for other phosphates such as $Ca_6Ba(PO_4)_4O$,[31] in agreement with the effect of halide ions in lowering the phonon energies of materials.

2.3. Luminescence Thermometry: From Boltzmann to Lifetime-Based Methods

To access the potential of this family of compounds as optical thermometers, the temperature dependence of the PL spectra was first investigated in the 77–500 K range (**Figure** 5a-c). The normalized spectra evidence the relative increase between the emission peaks coming from the split components of the ^1E state (labelled E_1 and E_2) as better emphasized in Figure 4a-c. As the temperature increases, the higher lying E_2 state increases with respect to the E_1 state. In addition to this spectral change, as the temperature increases, a growing broadband emission is observed at the base of the $^1E \rightarrow {}^3A_2$ transitions. This is assigned to the $^3T_2 \rightarrow {}^3A_2$ transition, as reported in other compounds.[19,31,33,36] This behavior allows to define two thermometric parameters based on (i) the ratio between the ^1E components $LIR_E = I_{E_2}/I_{E_1}$ and (ii) the ratio between the emission originating from the $^3T_2$ and ^1E states $LIR_{TE} = I_{^3T_2}/I_{^1E}$. In order to disclose whether the two couples of states used are in thermal equilibrium and, therefore, whether the thermometers follow the Boltzmann law $LIR = B \cdot exp(-\Delta E/k_B T)$, where B is the electronic constant, ΔE the energy gap between the two excited states, and k_B the Boltzmann constant, the corresponding Boltzmann plots of LIR versus $1/T$ were employed (Figure 5d-f). The range of linearity of the thermometers demonstrated their potential and the temperature range of applicability of the Boltzmann thermometers. The thermometers built from the ^1E split components follow the Boltzmann law in the whole temperature range explored for both the bromide and chloride samples, ensuring a high degree of reliability. In the case of $Sr_5(PO_4)_3F:Mn^{5+}$, at temperatures higher than 350 K, the overlap between the emissions originating from the ^1E split states makes the use of the thermometer difficult. From the linear trends, the energy gap between the E_1 and E_2 energy states ΔE_E is calculated to be 39 ± 2,

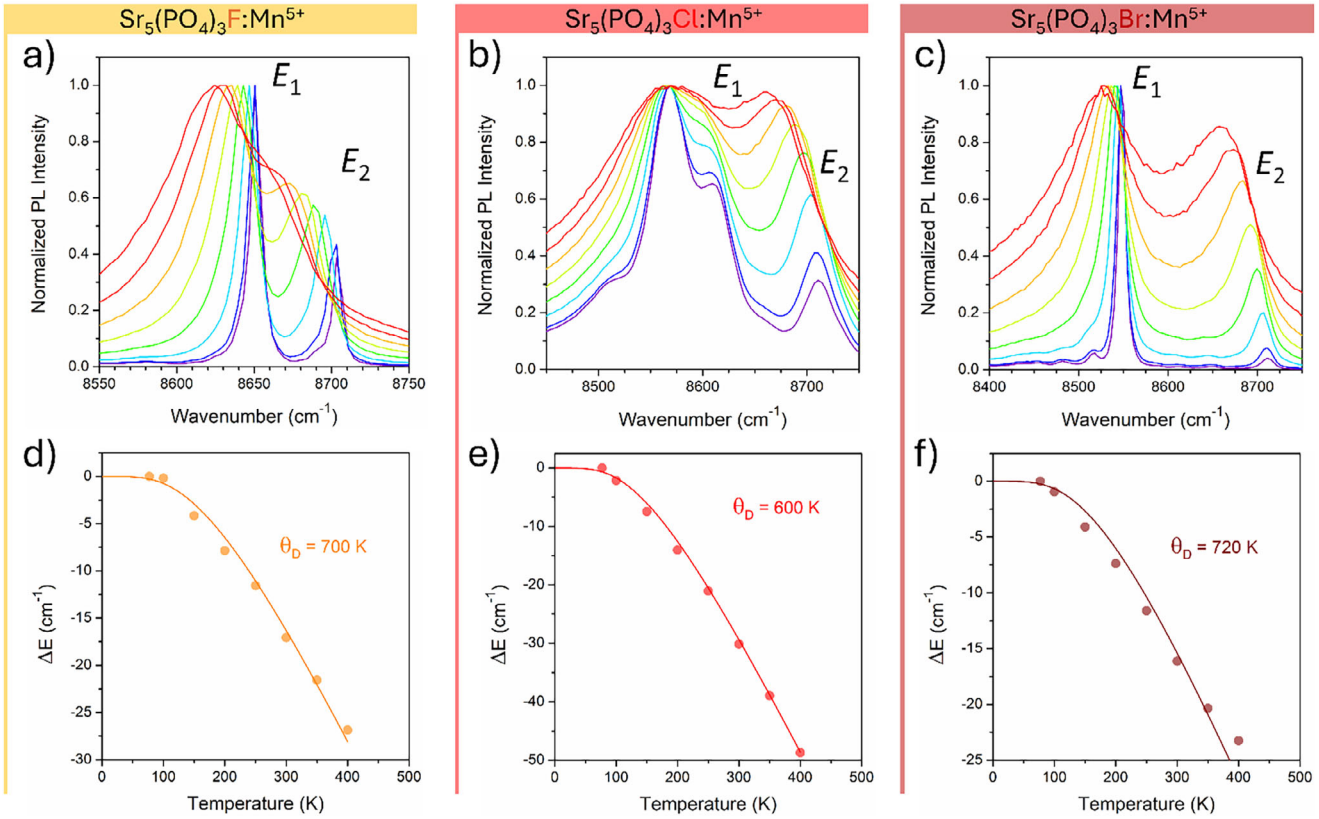

Figure 4. a-c) Spectral emission shift of the $^1E \rightarrow {}^3A_2$ peaks as a function of temperature in the 77–400 K range and d-f) temperature dependence of the energy shift of the E_1 line of Mn^{5+} with fit (solid line) using Equation (6).

80 ± 2, and 211 ± 7 cm^{-1} moving from the fluoride to the chloride and bromide samples, respectively. It is evident that there is a direct correlation between the ΔE_E energy gap and the distortion index D (Table S6, Supporting Information): the smaller the distortion index, the larger the energy gap between the E_1 and E_2 states.

Regarding the thermometers built by considering the ratio between the ^1E and $^3T_2$, it must be pointed out that the range of linearity of the Boltzmann law is much narrower than in the case of the LIR_E (200-500 K for bromide and chloride samples and 250–500 K for the fluoride apatite). This behavior can be explained considering the large energy gap between the excited states, resulting in a weak population of the higher lying $^3T_2$ state around room temperature. The ΔE_{TE} energy gaps are estimated to be 1160 ± 15 cm^{-1} for $Sr_5(PO_4)_3Br:Mn^{5+}$, 1000 ± 10 cm^{-1} for $Sr_5(PO_4)_3Cl:Mn^{5+}$, and 1517 ± 46 cm^{-1} for $Sr_5(PO_4)_3F:Mn^{5+}$.

Two of the most important parameters used to discuss the performance of the thermometers are the relative sensitivity (S_r), a figure of merit allowing the comparison among the thermometers of different nature, and the absolute sensitivity (S_a), defined as

$$S_a = \left| \frac{\partial LIR}{\partial T} \right| \tag{7}$$

$$S_r = \frac{1}{LIR} \left| \frac{\partial LIR}{\partial T} \right| \tag{8}$$

Figure 5g-i show the values of both relative and absolute sensitivities calculated in the range of linearity of the Boltzmann law for the two thermometers. For Boltzmann thermometers $S_r = \frac{\Delta E}{k_B T^2}$; therefore, the difference between the S_r values for the thermometers built considering LIR_{TE} and LIR_E reflects the differences in the energy gap between the couples of excited states. The values of relative sensitivity obtained for the LIR_{TE}, $S_{r,TE}$ are the highest values reported so far for Mn^{5+}-doped thermometers (see the comparison with the literature in Table S7, Supporting Information), with values at 300 K of 2.91%•K^{-1} for $Sr_5(PO_4)_3F:Mn^{5+}$, 2.05%•K^{-1} for $Sr_5(PO_4)_3Br:Mn^{5+}$, and 1.68%•K^{-1} for $Sr_5(PO_4)_3Cl:Mn^{5+}$. On the other hand, the use of LIR_E allows to expand the range of temperatures at which the S_r values are larger than 1%•K^{-1} to low temperatures showing unprecedent values in the case of the bromide apatite, where the $S_{r,E}$ values are all larger than 1%•K^{-1} for temperatures lower than 200 K with a maximum values of 4%•K^{-1} at 77 K (see Figure 5g).

It is important to recognize that, despite the recent proposal of the use of the $^3T_2/^1E$ PL intensity ratio for the physiological temperature range,[31,33,36] the large energy gap between the ^1E and $^3T_2$ excited states allows to only weakly populate the higher lying $^3T_2$ state around room temperature resulting in a weak broadband emission often emphasized by a logarithmic scale, making this strategy not particularly reliable due to the low signal-to-noise ratio. A similar situation is well known in the case of the Nd^{3+}-activated thermometers based on the ratio between the $^4F_{5/2} \rightarrow {}^4I_{9/2}$ and $^4F_{3/2} \rightarrow {}^4I_{9/2}$ transitions.[64,65] Therefore, the

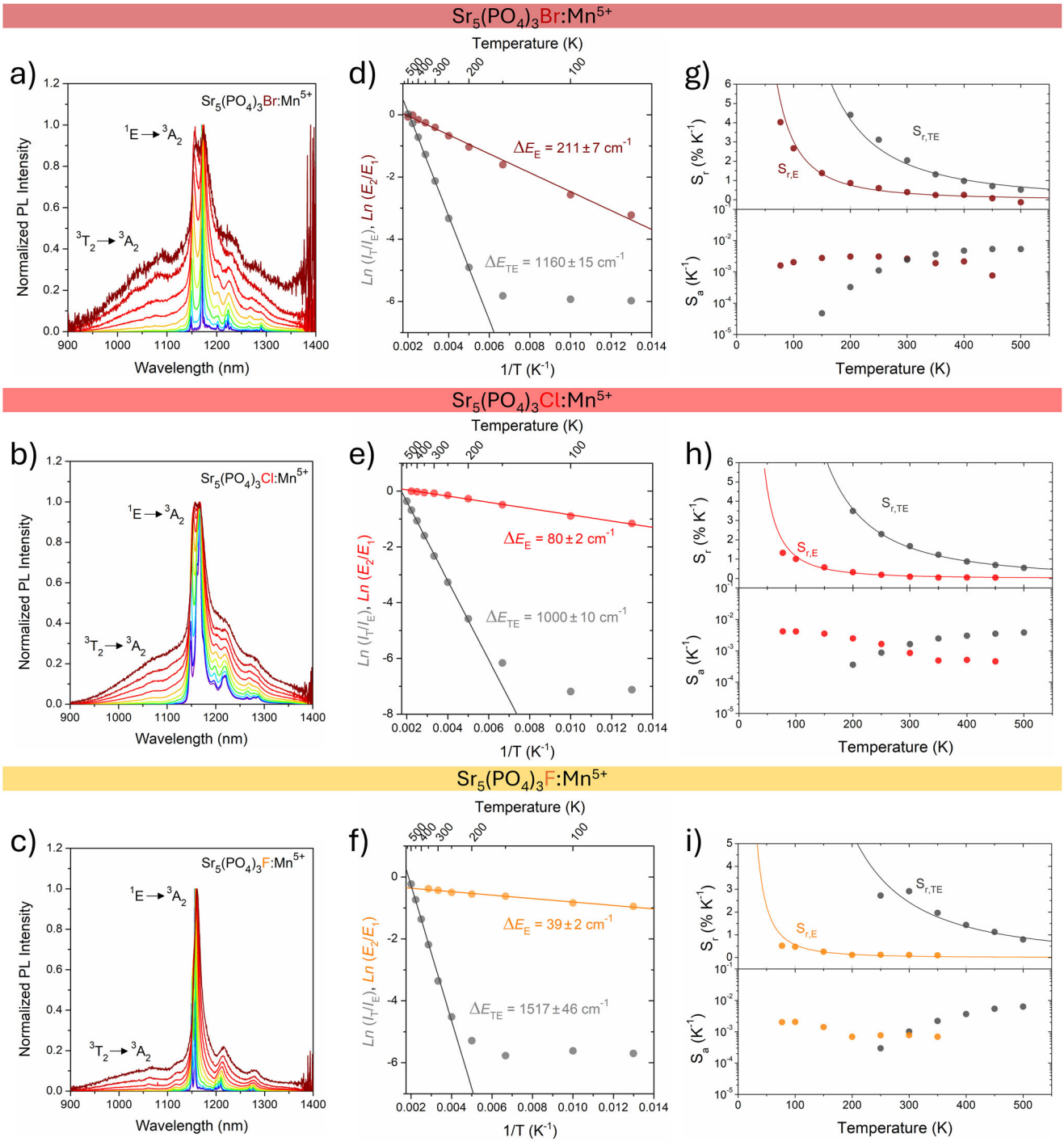

Figure 5. a-c) Normalized temperature-dependent PL spectra. d-f) Boltzmann plot for the thermometric parameters built considering the ratio between the $^3T_2$ and ^1E states (LIR_{TE}) and between E_2 and E_1 levels (LIR_E) along with the fit of the linear ranges. g-i) Absolute and relative sensitivities for the LIR-based thermometers and theoretical S_r (solid line) considering the corresponding ΔE estimated.

possibility to simultaneously use the $^3T_2/^1E$ and E_2/E_1 intensity ratio allows for expanding the temperature window of application of the thermometers in the whole temperature range explored. This makes the thermometers useful not only for biological applications but also for low and high temperatures, with relative sensitivities of both the LIR_{TE} and LIR_E thermometers, particularly promising for $Sr_5(PO_4)_3Br:Mn^{5+}$.

Looking for correlations between the sensitivities and geometric parameters that could be easily extrapolated from crystalline structure databases, such as the polyhedral distortion index D

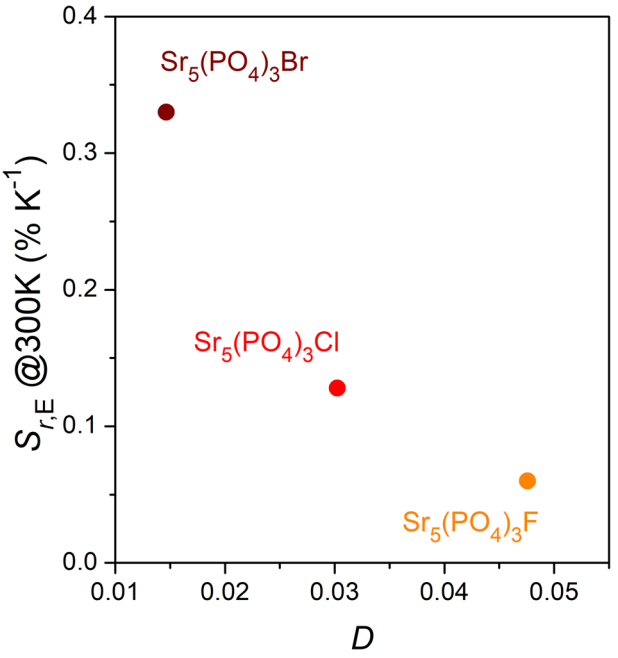

Figure 6. Correlation between the relative sensitivity $S_{r,E}$ at 300 K and the distortion index *D*.

and the angle distortion index δ, an inverse correlation between $S_{r,E}$, and the distortion index *D* can be observed (**Figure 6**).

Despite the reliability and the promising results obtained for the *LIR*-based technique using the $^3T_2$-^1E and E_1-E_2 excited state couples, it was demonstrated that the luminescence spectral shapes can be strongly affected by the biological environment with a clear limit in their applicability in the biological field.[66] In this view, the use of lifetimes is preferred. Therefore, the temperature dependence of the PL decay curves is investigated (**Figure** 7a-c). The decays were fitted with a single exponential to extrapolate the lifetime of the excited state. The Mott-Seitz model (single-barrier energy gap model) was employed to describe the temperature dependence of the lifetime

$$\tau(T) = \frac{\tau_0}{1 + C \cdot \exp\left(\frac{-\Delta E_{nr}}{k_B T}\right)} \quad (9)$$

where τ_0 is the radiative luminescence lifetime, $C = k_{nrad}/k_{rad}$ is the ratio between the non-radiative and radiative decay rates, ΔE_{nr} is the energy gap between the emitting level and the closest lower-lying energy level, and k_B is the Boltzmann constant. The fit of the temperature-dependent lifetime measurements (Figure 7d-f) allows to estimate an energy barrier of 1485 ± 75 cm^{-1}, 1430 ± 60 cm^{-1}, and 1315 ± 90 cm^{-1} for the bromide, chloride, and fluoride apatites, respectively.

The $\Delta E_{TE,\tau}$ value obtained for the $Sr_5(PO_4)_3Cl:Mn^{5+}$ sample of 1430 ± 60 cm^{-1} is, within the errors, the same reported by Oetliker et al.[6] (1450 cm^{-1}), ensuring the reliability of the analysis.

As for the *LIR*-based thermometers, the absolute sensitivity $S_{a,\tau} = |\frac{\partial \tau}{\partial T}|$ and the relative sensitivity $S_{r,\tau} = \frac{1}{\tau}|\frac{\partial \tau}{\partial T}|$ were calculated as reported in Figure 7g-i.

A relative sensitivity $S_{r,\tau}$ of 0.42%•K^{-1} was reported at 300 K for $Ba_3(VO_4)_2$,[34] 0.35%•K^{-1} for $Ba_5(VO_4)_3Cl$,[36] 0.30%•K^{-1} for $Ba_3(PO_4)_2$,[32] and 0.40%•K^{-1} for $Sr_3(PO_4)_2$.[32] As summarized in Table S7 (Supporting Information), the values of 0.61 %•K^{-1} estimated at 300 K for both $Sr_5(PO_4)_3Br:Mn^{5+}$ and $Sr_5(PO_4)_3Cl:Mn^{5+}$ are the highest reported in literature for the NIR emitting Mn^{5+}-doped thermometers.

Among the Mn^{5+}-activated phosphors reported so far in literature (Table S7, Supporting Information), $Sr_5(PO_4)_3Br:Mn^{5+}$ is one of the most promising, combining high quantum yield with one of the highest relative sensitivities for the thermometers built by using the $^3T_1/^1E$ ratio (2.05%•K^{-1} at 300 K) and the E_2/E_1 ratio (0.33 %•K^{-1} at 300 K) and the highest among the PL lifetime-based thermometers in the physiological range (0.61 %•K^{-1} at 300 K). Moreover, $Sr_5(PO_4)_3Cl:Mn^{5+}$ can also be considered a suitable candidate for real applications by using the τ-based technique, characterized by a relative sensitivity comparable to the bromide sample.

The obtained results show how to expand the working temperature range of Mn^{5+}-based thermometers by taking advantage of the ^1E splitting. They also make it possible to predict the energy gap and, therefore, the sensitivity of the Boltzmann thermometer based on these thermally coupled excited states, by considering a geometric parameter (distortion index *D*), predictable from structural information and existing databases. Overall, this work lays the foundation for future research directions in this field.

3. Conclusion

In conclusion, the structure-optical properties relationship in the NIR emitting $Sr_5(PO_4)_3X:Mn^{5+}$ (X = Br, Cl, and F) apatite phosphors was investigated by combining an experimental and theoretical approach. The effect of the local tetrahedral oxygen shell on the 3d2 electrons of Mn^{5+} ions was studied by means of the Tanabe-Sugano theory and the exchange charge model of the crystal field theory, showing the strong effect of the tetrahedral distortion. Temperature-dependent PL measurements were carried out in the 77–500 K range to address the potential of the phosphors as ratiometric luminescent thermometers. The use of two Boltzmann thermometers based on the ratio between the $^3T_2$ and ^1E PL emissions (LIR_{TE}) and the split components of ^1E, E_1 and E_2 (LIR_E) ensures a high reliability in a wide temperature range, overcoming the limit of the LIR_{TE}-based Mn^{5+} thermometers around the physiological range due to the weak $^3T_2 \rightarrow {}^3A_2$ transition expanding the temperature range.

Based on the NIR emission and excitation, Mn^{5+}-doped phosphors are considered particularly suitable for biological applications. The most reliable lifetime-based thermometry technique was employed, showing the highest relative sensitivity reported so far (0.61%•K^{-1} at 300 K) for both $Sr_5(PO_4)_3Br:Mn^{5+}$ and $Sr_5(PO_4)_3Cl:Mn^{5+}$ apatite. Moreover, considering the high quantum yield (66%), the highest relative sensitivity among the apatites for the LIR_E-based thermometers (4%•K^{-1} at 77 K), one of the highest value for LIR_{TE}-based (2.05%•K^{-1} at 300 K) and the lifetime-based thermometry, $Sr_5(PO_4)_3Br:Mn^{5+}$ is considered a promising candidate for real applications. Finally, a correlation between the E_1-E_2 energy gap, and, therefore, the sensitivity of the LIR_E-based thermometers, and the distortion index *D* was

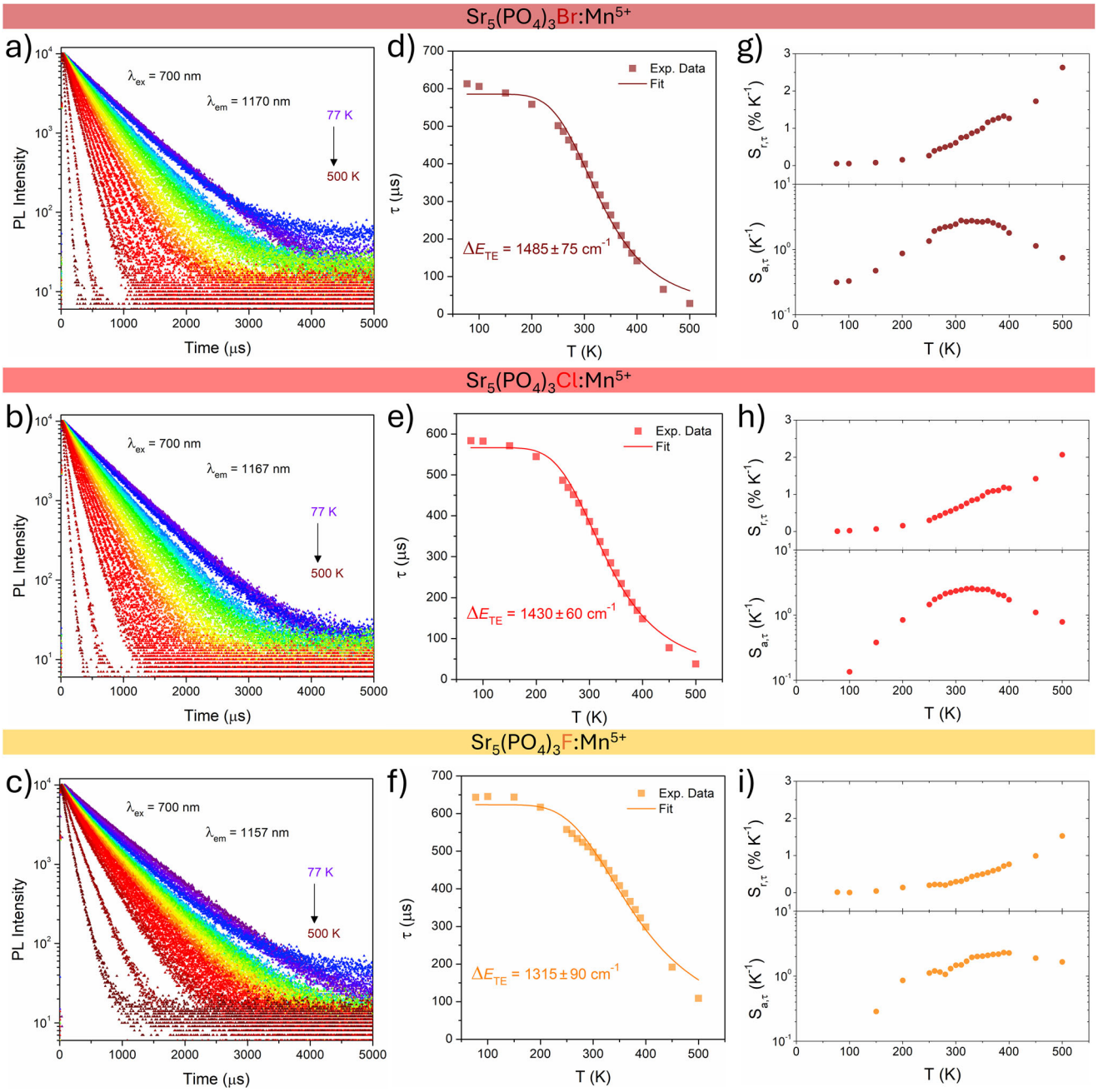

Figure 7. Temperature dependence of a-c) PL decay curves, d-f) lifetimes with single-barrier energy gap model fit (Equation 9), and g-i) absolute $S_{a,\tau}$ and relative $S_{r,\tau}$ sensitivities.

disclosed, allowing the prediction of suitable hosts based on structural information.

4. Experimental Section

Synthetic Procedure: The synthesis of Mn^{5+}-doped $Sr_5(PO_4)_3X$ (X = F, Cl, Br) was performed by a two-step procedure. In the first step, $Sr_3(PO_4)_2$ powder was synthesized by the wet precipitation method, followed by high-temperature annealing (the purity was verified by XRD analysis, Figure S4, Supporting Information). During the second step, three series of Mn^{5+}-doped $Sr_5(PO_4)_3X$ (X = F, Cl, Br) powders were synthesized by the molten salt method. In a typical procedure, 1 g of $Sr_3(PO_4)_2$ was thoroughly mixed with a certain amount of $Mn(NO_3)_2 \cdot 4H_2O$ (≥98%, Roth) and an appropriate metal halide salt. The mass ratio between precursors and flux was chosen as 1:2 (calculated with respect to anhydrous salt). $SrCl_2$ (≥95%, Thermo Scientific) and $SrBr_2 \cdot 6H_2O$, (≥99%, Thermo Scientific) were used for the synthesis of $Sr_5(PO_4)_3Cl$ and $Sr_5(PO_4)_3Br$, respectively. For the synthesis of $Sr_5(PO_4)_3F$, a mixture of SrF_2 (≥99%, Thermo Scientific) and NaF (≥99%, Scharlau) with a molar ratio of 0.025:0.975 was used. Manganese precursor was added according to a nominal Mn substitution level from 1 to 5 mol% with respect to P^{5+} ions. The obtained mixture

was transferred into the corundum crucible, covered with a lid, and annealed at an appropriate temperature for 5 h in air with a heating rate of 5 °C/min. The annealing temperature was 1050 °C, 1050 °C and 700 °C for $Sr_5(PO_4)_3F$, $Sr_5(PO_4)_3Cl$ and $Sr_5(PO_4)_3Br$, respectively. After the annealing procedure, the furnace was allowed to cool down naturally. The obtained products were washed with hot deionized water to dissolve residual metal halides. All powders were then dried in an oven at 80 °C and ground in an agate mortar.

Structural and Optical Characterizations: X-ray diffraction patterns (XRD) were collected at room temperature using an Empyrean diffractometer (Malvern Panalytical) with Bragg-Brentano para focusing geometry equipped with a PIXcel3D-Medipix3 1×1 area detector and Cu– Kα radiation ($\lambda = 1.5418$ Å), with a scan rate of 1°/80 sec at 40 kV and 40 mA with continuous acquisition lasting 300 seconds. In order to consider the preferred orientation of the materials prepared, the March-Dollase function was employed:[54,55]

$$W(\alpha) = \left(r_n^2 cos^2\alpha_{n,h} + r_n^{-1} sin^2\alpha_{n,h}\right)^{-3/2} \quad (10)$$

where $\alpha_{n,h}$ is the angle between the orientation vector and diffraction plane vector, and r_n is the March number determining the preferred orientation strength. When $r_n = 1$, no preferred orientation is present, while $r_n<1$ and $r_n>1$ are characteristic of a preferred orientation by plate crystallites and needle crystallites, respectively.

The room temperature and temperature-dependent (77 – 500 K range) excitation and emission spectra and PL decay curves were recorded using an Edinburgh Instruments FLS980 spectrometer (Edinburgh Instruments, Livingston, UK) equipped with double-grating Czerny-Turner excitation and emission monochromators. For steady-state measurements, a 450 W ozone-free xenon arc lamp (Osram, Germany) was used as the excitation source. For the kinetic measurements, a micro flash lamp (μF2) was used as the excitation source. The emission in the UV-Vis spectrum was detected using a Hamamatsu R928P photomultiplier (cooled to −20 °C). Emission in the NIR range was detected using a Hamamatsu R5509-42 photomultiplier (cooled to −80 °C). Emission spectra were corrected for the spectral response of the instrument. The excitation spectra were corrected using a reference detector. A MicrostatN cryostat (Oxford Instruments) was used for temperature-dependent measurements. The samples were cooled with liquid nitrogen.

Quantum efficiencies (QE) were measured by a direct method employing Teflon coated integrating sphere and using barium sulfate as a white standard ($BaSO_4$ for white standard DIN 5033, Merck). QE was calculated using the following equation:[67]

$$QE = \frac{\int I_{em,sample} - \int I_{em,BaSO_4}}{\int I_{refl,BaSO_4} - \int I_{refl,sample}} \times 100\% = \frac{N_{em}}{N_{abs}} \times 100\% \quad (11)$$

where $\int I_{em,\ sample}$ and $\int I_{refl,\ sample}$ are integrated emission and reflectance of the sample, respectively. $\int I_{em,\ BaSO4}$ and $\int I_{refl,\ BaSO4}$ are integrated emission and reflectance of the barium sulfate standard. N_{em} and N_{abs} stand for emitted and absorbed photons, respectively.

Supporting Information

Supporting Information is available from the Wiley Online Library or from the author.

Acknowledgements

This project has received funding from the Research Council of Lithuania (LMTLT), agreement No S-MIP-23-85. This work has also benefited from the infrastructural support of the Centre for Trace Analysis (CeTrA) of Ca' Foscari University through the project IR0000032 – ITINERIS, Italian Integrated Environmental Research In-frastructures System, funded by EU – Next Generation EU, PNRR- Mission 4 "Education and Research" – Component 2: "From research to business" – Investment 3.1: "Fund for the realisation of an integrated system of research and innovation infrastructures". M.G.B. thanks the support from the Specialized Funding Program for the Gathering of 100 Elite Talents in Chongqing and the Overseas Talents Plan (Grant No. 2022[60]) both offered by Chongqing Association for Science and Technology, the Polish NCN project 2023/49/B/ST5/03384, the Estonian Research Council grant (PRG 2031), and the Ministry of Science, Technological Development, and Innovation of the Republic of Serbia under contract 451-03-47/2023−01/200017.

Open access publishing facilitated by Universita Ca' Foscari, as part of the Wiley - CRUI-CARE agreement.

Conflict of Interest

The authors declare no conflict of interest.

Data Availability Statement

The data that support the findings of this study are available from the corresponding author upon reasonable request.

Keywords

apatite, distortion index, Mn5+, near-infrared, phosphors, thermometry

Received: September 21, 2025
Revised: December 1, 2025
Published online: December 29, 2025

[1] W. Klemm, *Angew. Chem.* **1954**, *66*, 468.
[2] R. Scholder, W. Klemm, *Angew. Chem.* **1954**, *66*, 461.
[3] D. Reinen, H. Lachwa, R. Allmann, *Z. Anorg. Allg. Chem.* **1986**, *542*, 71.
[4] H. Lachwa, D. Reinen, *Inorg. Chem.* **1989**, *28*, 1044.
[5] S. Kuzman, T. Dramicanin, A. I. Popov, M. G. Brik, M. D. Dramicanin, *Nanomaterials* **2025**, *15*, 275.
[6] U. Oetliker, M. Herren, H. U. Güdel, U. Kesper, C. Albrecht, D. Reinen, *J. Chem. Phys.* **1994**, *100*, 8656.
[7] J. D. Kingsley, J. S. Prener, B. Segall, *Phys. Rev.* **1965**, *137*, A189.
[8] R. Borromei, L. Oleari, P. Day, *J. Chem. Soc., Faraday Trans. 2* **1977**, *73*, 135.
[9] M. Herren, H. U. Güdel, C. Albrecht, D. Reinen, *Chem. Phys. Lett.* **1991**, *183*, 98.
[10] J. A. Capobianco, G. Cormier, M. Bettinelli, R. Moncorgé, H. Manaa, *J. Lumin.* **1992**, *54*, 1.
[11] J. A. Capobianco, G. Cormier, R. Moncorgé, H. Manaa, M. Bettinelli, *Appl. Phys. Lett.* **1992**, *60*, 163.
[12] C. Albrecht, S. Cohen, I. Mayer, D. Reinen, *J. Solid State Chem.* **1993**, *107*, 218.
[13] L. C. Ferracin, M. R. Davolos, L. A. O. Nunes, *J. Lumin.* **1997**, *72–74*, 185.
[14] D. Reinen, W. Rauw, U. Kesper, M. Atanasov, H. U. Güdel, M. Hazenkamp, U. Oetliker, *J. Alloys Compd.* **1997**, *246*, 193.
[15] T. Riedener, Y. Shen, R. J. Smith, K. L. Bray, *Chem. Phys. Lett.* **1991**, *183*, 445.
[16] M. G. Brik, E. Cavalli, R. Borromei, M. Bettinelli, *J. Lumin.* **2009**, *129*, 801.
[17] Y. Shen, T. Riedener, K. L. Bray, *Phys. Rev. B* **2000**, *61*, 9277.
[18] X. Zhang, J. Nie, S. Liu, J. Qiu, *J. Mater. Sci.: Mater. Electron.* **2018**, *29*, 6419.

[19] W. Huang, C. Li, L. Zeng, J. Zhang, M. A. Kurochkin, I. E. Kolesnikov, Z. Umar, J. Zhang, W. Liu, A. Kukovecz, M. S. Kurboniyon, X. Zhang, *Inorg. Chem.* **2025**, *64*, 12100.
[20] M. A. Noginov, G. B. Loutts, N. Noginova, S. Hurling, S. Kück, *Phys. Rev. B* **2000**, *61*, 1884.
[21] M. G. Brik, I. Sildos, M. Berkowski, A. Suchocki, *J. Phys.: Condens. Matter.* **2009**, *21*, 025404.
[22] L. D. Merkle, H. R. Verdun, B. McIntosh, In *OSA Proceedings on Advanced Solid-State Larers* **1993**.
[23] M. F. Hazenkamp, H. U. Güdel, S. Kück, G. Huber, W. Rauw, D. Reinen, *Chem. Phys. Lett.* **1997**, *265*, 264.
[24] S. Kück, K. L. Schepler, B. H. T. Chai, *J. Opt. Soc. Am. B* **1997**, *14*, 957.
[25] M. A. Scott, T. P. J. Han, H. G. Gallagher, B. Henderson, *J. Lumin.* **1997**, *72–74*, 260.
[26] A. A. Kaminskii, *Phys. Stat. Sol. a* **2003**, *200*, 215.
[27] L. D. Merkle, A. Pinto, H. R. Verdun, B. McIntosh, *Appl. Phys. Lett.* **1992**, *61*, 2386.
[28] P. M. Gschwend, K. Keevend, M. Aellen, A. Gogos, F. Krumeich, I. K. Herrmann, S. E. Pratsinis, *J. Mater. Chem. B* **2021**, *9*, 3038.
[29] V. Rajendran, K.-C. Chen, W.-T. Huang, N. Majewska, T. Lesniewski, M. Grzegorczyk, S. Mahlik, G. Leniec, S. M. Kaczmarek, W. K. Pang, V. K. Peterson, K.-M. Lu, H. Chang, R.-S. Liu, *ACS Energy Lett.* **2023**, *8*, 289.
[30] P. M. Gschwend, D. Niedbalka, L. R. H. Gerken, I. K. Herrmann, S. E. Pratsinis, *Adv. Sci.* **2020**, *7*, 2000370.
[31] M. D. Dramicanin, L. Marciniak, S. Kuzman, W. Piotrowski, Z. Ristic, J. Perisa, I. Evans, J. Mitric, V. Dordevic, N. Romcevic, M. G. Brik, C.-G. Ma, *Light Sci. Appl.* **2022**, *11*, 279.
[32] Z. Ristic, W. Piotrowski, M. Medic, J. Perisa, Z. M. Antic, L. Marciniak, M. D. Dramicanin, *ACS Appl. Electron. Matter.* **2022**, *4*, 1057.
[33] T. A. Alrebdi, A. N. Alodhayb, Z. Ristic, M. D. Dramicanin, *Sensors* **2023**, *23*, 3839.
[34] W. M. Piotrowski, R. Marin, M. Szymczak, E. M. Rodriguez, D. H. Ortgies, P. Rodriguez-Sevilla, M. D. Dramicanin, D. Jaque, L. Marciniak, *Adv. Optical Mater.* **2023**, *11*, 2202366.
[35] W. Huang, J. Zhang, Y. Zheng, L. Zeng, W. Liu, Z. Umar, M. Xie, Y. Bokshyts, J. Pan, X. Zhang, *Dalton Trans.* **2024**, *53*, 10261.
[36] W. Huang, J. Zhang, J. Fan, J. Zhang, J. Huang, P. Chen, L. Zhou, X. Zhang, *Acta Mater.* **2024**, *273*, 119981.
[37] X. Yan, S. Su, Z. Chen, Y. Jia, Y. Li, E. Song, Q. Zhang, *ACS Appl. Electron. Mater.* **2025**, *7*, 8260.
[38] C. D. S. Brites, S. Balabhadra, L. D. Carlos, *Adv. Opt. Mater.* **2018**, *7*, 1801239.
[39] M. Quintanilla, L. M. Liz-Marzan, *Nano Today* **2018**, *19*, 126.
[40] M. D. Dramicanin, *J. Appl. Phys.* **2020**, *128*, 040902.
[41] F. Vetrone, R. Naccache, A. Zamarrón, A. Juarranz de la Fuente, F. Sanz-Rodríguez, L. Martinez Maestro, E. Martín Rodriguez, D. Jaque, J. García Solé, J. A. Capobianco, *ACS Nano* **2010**, *4*, 3254.
[42] M. Suta, *Nanoscale* **2025**, *17*, 7091.
[43] A. Benayas, B. del Rosal, A. Pérez-Delgado, K. Santacruz-Gomez, D. Jaque, A. Hirata, F. Vetrone, *Adv. Optical Mater.* **2015**, *3*, 687.
[44] S. Balabhadra, M. L. Debasu, C. D. S. Brites, L. A. O. Nunes, O. L. Malta, J. Rocha, M. Bettinelli, L. D. Carlos, *Nanoscale* **2015**, *7*, 17261.
[45] M. Back, E. Trave, J. Ueda, S. Tanabe, *Chem. Mater.* **2016**, *28*, 8347.
[46] M. Back, J. Ueda, J. Xu, K. Asami, M. G. Brik, S. Tanabe, *Adv. Optical Mater.* **2020**, *8*, 2000124.
[47] K. Okabe, N. Inada, C. Gota, Y. Harada, T. Funatsu, S. Uchiyama, *Nat. Commun.* **2012**, *3*, 705.
[48] M. Suzuki, T. Plakhotnik, *Biophys. Rev.* **2020**, *12*, 593.
[49] T. Hartman, R. G. Geitenbeek, C. S. Wondergem, W. van der Stam, B. M. Weckhuysen, *ACS Nano* **2020**, *14*, 3725.
[50] R. Vogel, D. W. Groefsema, M. A. van den Bulk, T. S. Jacobs, P. T. Prins, F. T. Rabouw, B. M. Weckhuysen, *ACS Appl. Mater. Interfaces* **2025**, *17*, 21215.
[51] M. Back, J. Ueda, H. Nambu, M. Fujita, A. Yamamoto, H. Yoshida, H. Tanaka, M. G. Brik, S. Tanabe, *Adv. Opt. Mater.* **2021**, *9*, 2100033.
[52] R. G. Geitenbeek, J. C. Vollenbroek, H. M. H. Weijgertze, C. B. M. Tregouet, A.-E. Nieuwelink, C. L. Kennedy, B. M. Weckhuysen, D. Lohse, A. van Blaaderen, A. van den Berg, M. Odijk, A. Meijerink, *Lab Chip* **2019**, *19*, 1236.
[53] R. Cao, X.-G. Yu, X. Sun, Z. Li, H. Zhang, Z. Liu, *Spectrochim. Acta Part A* **2014**, *130*, 671.
[54] A. March, *Cryst. Mater.* **1932**, *81*, 285.
[55] W. A. Dollase, *J. Appl. Crystallogr.* **1986**, *19*, 267.
[56] W. H. Baur, *Acta Crystallogr. Sect. B* **1974**, *30*, 1195.
[57] E. Hemmer, A. Benayas, F. Légaré, F. Vetrone, *Nanoscale Horiz.* **2016**, *1*, 168.
[58] M. Crozzolin, C. Belloni, J. Xu, T. Nakanishi, J. Ueda, S. Tanabe, F. Dallo, E. Balliana, A. Saorin, F. Rizzolio, D. Cristofori, P. Riello, A. Benedetti, M. Back, *J. Mater. Chem. C* **2024**, *12*, 10929.
[59] M. Back, J. Ueda, M. G. Brik, S. Tanabe, *ACS Appl. Mater. Interfaces* **2020**, *12*, 38325.
[60] B. Z. Malkin, A. A. Kaplyanskii, B. M. Macfarlane, *Spectroscopy of Solids Containing Rare-Earth Ions*, North-Holland, Amsterdam **1987**.
[61] M. G. Brik, C.-G. Ma, *Theoretical Spectroscopy of Transition Metal and Rare Earth Ions: From Free State to Crystal Field*, Jenny Stanford Publishing, Singapore **2020**.
[62] M. G. Brik, N. M. Avram, C. N. Avram, C. Rudowicz, Y. Y. Yeung, P. Gnutek, *J. Alloys Compd.* **2007**, *432*, 61.
[63] D. E. McCumber, M. D. Sturge, *J. Appl. Phys.* **1963**, *34*, 1682.
[64] M. Back, J. Xu, J. Ueda, S. Tanabe, *J. Ceram. Soc. Jpn.* **2023**, *131*, 57.
[65] M. Suta, Z. Antić, V. Đorđević, S. Kuzman, M. D. Dramićanin, A. Meijerink, *Nanomaterials* **2020**, *10*, 543.
[66] Y. Shen, J. Lifante, N. Fernández, D. Jaque, E. Ximendes, *ACS Nano* **2020**, *14*, 4122.
[67] J. Grigorjevaite, A. Katelnikovas, *ACS Appl. Mater. Interfaces* **2016**, *8*, 31772.